

Eleventh U.S. National Conference on Earthquake Engineering

Integrating Science, Engineering & Policy June 25-29, 2018 Los Angeles, California

3D models of the Leader Valley using satellite & UAV imagery following the 2016 Kaikoura earthquake

Zekkos, D.¹, Clark, M.², Willis, M.³, Athanasopoulos-Zekkos, A.⁴, Manousakis, J.⁵, Knoper, L.⁶, Stahl, T.⁷, Massey, C.⁸, Archibald, G.⁹, Greenwood, W.¹⁰, and Medwedeff, W.¹¹

ABSTRACT

The ability to quickly, efficiently and reliably characterize changes in the landscape following an earthquake has remained a challenge for the earthquake engineering profession. The 2016 M_w7.8 Kaikoura earthquake provided a unique opportunity to document changes in topography following an earthquake on a regional scale using satellite derived high-resolution digital models. Along-track stereo satellite imagery had been collected for the pre-event topography. Satellites were tasked and collected stereo-mode post-event imagery. Both sets of images were used to create digital surface models (DSMs) of the affected area before and after the event. The procedure followed and indicative results for the Leader valley are presented with emphasis on the challenges associated with the implementation of the technique for the first time in this environment. The valley is of interest because of the variety of features it includes, i.e., the large Leader landslide, smaller landslides, stable sloping and flat ground as well as fault rupture lineaments. The open-source SETSM software is used to provide multiple DSMs. Our workflow is described and results are compared against the DSM created using Structure-from-Motion with imagery collected by Unmanned Aerial Vehicles (UAV) and aerial LIDAR. Overall, the sub-meter agreement between the DSM created using satellites and the DSM created using UAV and LIDAR datasets demonstrates viability for use in seismic studies, but features smaller than about 0.5 m are more difficult to discern.

¹ Associate Professor, Dept. of Civil and Environmental Engineering, University of Michigan, 2350 Hayward Str. Ann Arbor, MI, 48109 (e-mail: zekkos@geoengineer.org)

² Associate Professor, Dept. of Earth & Environmental Science, University of Michigan, 2534 1100 North University Building, 1100 North University Avenue, Ann Arbor, MI 48109

³ CIRES Fellow & Assistant Professor, Dept. of Geological Science, Univ. of Colorado, UCB399, Boulder, CO 80309

⁴ Associate Professor, Dept. of Civil and Environmental Engineering, University of Michigan, 2350 Hayward Str. Ann Arbor, MI, 48109

⁵ Geomatics Engineer, Elxis Group, Dimitressa 7-9 Athens, 115 28, Greece.

⁶ Research Assistant, Dept. of Earth & Environmental Science, University of Michigan, 2534 1100 North University Building, 1100 North University Avenue, Ann Arbor, MI 48109

⁷ Lecturer, University of Canterbury, New Zealand

⁸ Engineering Geologist, GNS Science, New Zealand

⁹ Engineering Geological Surveyor, GNS Science, New Zealand

¹⁰ PhD student, Dept. of Civil & Environm. Engin., Univ. of Michigan, 2350 Hayward Str. Ann Arbor, MI, 48109

¹¹ PhD student, Dept. of Earth & Environmental Science, University of Michigan, 2534 1100 North University Building, 1100 North University Avenue, Ann Arbor, MI 48109

Introduction

On November 14 (local time) 2016, a $M_w7.8$ earthquake event ruptured several faults along the coastal portion of the Canterbury and Marborough regions of New Zealand. The event was unusual in the number of individual fault segments that ruptured, the large distances over which fault slip was transferred between individual segments, and the possible simultaneity of subduction interface slip with shallow crustal faults. Rupture initiated on the Humps fault, ~120 km NE of the 2011 Darfield earthquake sequence that affected Christchurch. Rupture propagated northnortheastward through a sequence of primarily dextral strike-slip and reverse fault structures, including the Humps, Hundalee, and Kekerengu faults, but other significant faults slipped with sinistral reverse motion (e.g. Papatea fault). Measured slip offsets from field observation immediately following the earthquake are commonly 1-3 m and reached a maximum of 12 m dextral offset on the Kekerengu fault (Hamling et al. 2017).

The area of fault rupture occurred primarily within high-relief, strongly dissected mountainous topography as well as along a steep coastal margin. Strong ground motions exceeding 1g (GEER 2017) initiated widespread landsliding (n > 10,000) (Massey et al. 2017, Dellow et al. 2017). Such a large landsliding event is common with shallow rupture of continental faults, which typically can cause up to several tens of thousands of shallow rock slides on steep gradients of weathered/fractured rock and soil. However, larger, deep-seated landslides, which were less frequent, are of particular note. These slides dammed rivers (n > 200), some of which (n > 10) threatened potential flood conditions for downstream communities within the past year since the earthquake event. Notably, these larger landslides mostly occurred within younger Tertiary strata. While their size and interaction with the fluvial network elevated the threat associated with this particular style of landsliding, there was also a possible relationship of surface faulting and the initiation of these particular failures.

In this paper we evaluate the uncertainties within high-resolution topographic models derived from satellite-based photogrammetry and their suitability for determining earthquake-related surface changes. We focus on one area, the Leader valley, where a large landslide occurred (shown in Fig. 1) adjacent to the Leader fault rupture and formed a temporary landslide dam across the Leader river. Post-event digital surface models are developed using three different methods, along with a difference model derived from pre- and post-event satellite-based models. Satellite DSMs are differenced from LiDAR DEMs and UAV photogrammetry-based DSMs to determine average and spatial patterns of misfit over specific features. Before- and after-event satellite models are differenced so that landslide and fault offsets can be compared to field measurements.

Data Acquisition & Analysis Methods

Satellite-based SETSM Surface Extraction with TIN-based Search-space Minimization

Along-track stereo satellite imagery had been collected across much of the South Island of New Zealand following the 2010 Darfield and 2011 Christchurch earthquakes. The imagery used in this study is from March 23 2015. Additional satellite imagery was acquired soon after the November 14 2016 Kaikoura earthquake, i.e., on December 29 2016, and an additional dataset from May 25 2017 was also used. An archive of approximately one hundred stereo swaths covers the region of interest around Kaikoura from before the main event. These were processed using the Bluewaters Petascale computing facility to produce digital surface models of half-meter and two meter postings. About one hundred stereo swaths from after the event have been processed to the same postings. We use the open source Surface Extraction with TIN-based Search-space minimization

(SETSM) methodology (vers. 3.2.7) developed by Noh and Howat (2015; 2017), which is based on a combination of the vertical line locus method (Schenk, 1999) and an adjustment of the rational polynomial coefficients that describe the satellite orbit in order to produce surface models. Overlapping tiles from each of the stereo swaths are first corrected for sensor aberrations using tools from the Ames Stereo Pipeline (Shean et al. 2016). The workflow then queues the tile-pairs for processing. Typical accuracy, after ground control is applied, for these DigitalGlobe Satellite derived DSMs is 0.25-0.5m (e.g. Shean et al. 2016; Willis et al. 2015).

DSM registration of before and after scenes is performed by applying a transformation based on the Iterative Closest Point (ICP) method in Cloud Compare. This method calculates a rigid body transformation between two terrain models that minimizes the closest point distances between them as defined by a matrix composed of translations (t_x , t_y and t_z in the x, y, z direction) and rotations (α , β , γ about the x, y, z axes). The transformation matrix is then applied to one DSM and the point-wise difference between the reference and the transformed DSM is calculated. We use this method in two ways. First, difference calculations between reference datasets (LiDAR and UAV-SfM) and the satellite based DSM are evaluated for model performance of the satellite-based terrain data. Second, difference maps between before, and one month after and/or six months after the earthquake are used to determine the accuracy with which surface change can be measured compared to features in the reference datasets and field measurements.

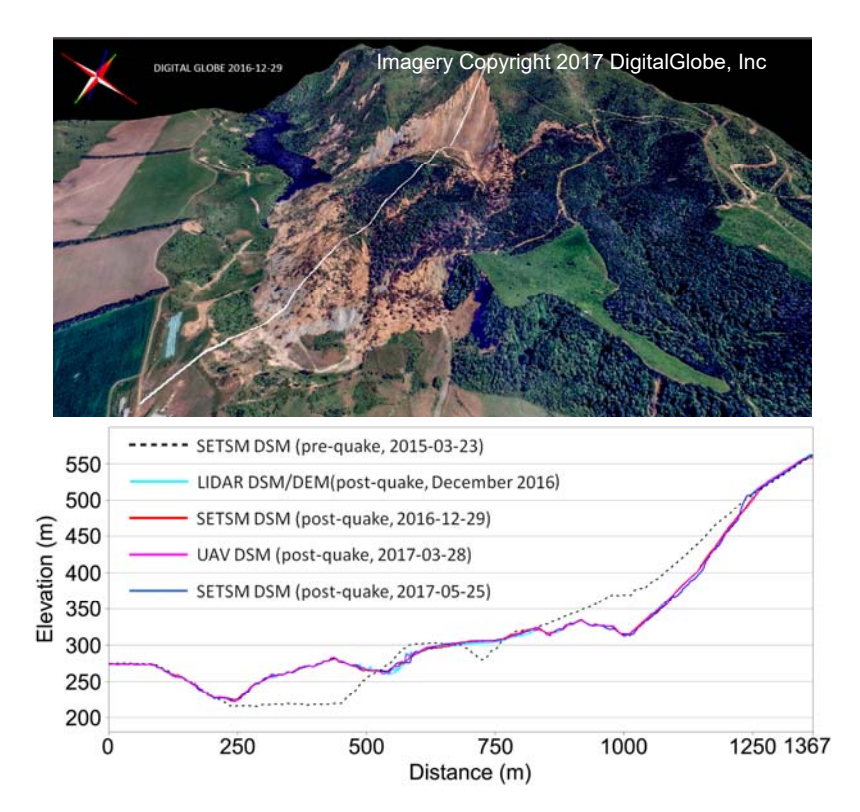


Figure 1. (a) Oblique view of the Leader landslide and (b) cross-section through the landslide and valley using various mapping techniques.

UAV-based Structure-from-Motion (SfM) DSM

The study area was also mapped during field deployment on 28-30 March 2017. The DJI Phantom 4 Pro Unmanned Aerial Vehicle (UAV) was used to collect Ultra-High Definition imagery using

a 20 MP camera. For the majority of the study area, still images were collected in plan view using a series of autonomous lawn-mower type flight paths. In addition, side-view video was collected of the back-scarp of the landslide and images were extracted of the video to use in the analysis. This was needed, because flying above the back-scarp of the landslide from the take-off location would have required flight elevations greater than 400 m that were not considered safe. In total 14 flight paths were conducted for a total of 280 minutes to map the target plan area of 2.2 km². A total of 7815 geo-located overlapping images were used as input in the Structure-from-Motion analyses. The software Pix4D was used for the analyses. The SfM methodology uses Scale Invariant Feature Transformation (SIFT) algorithms applied to feature descriptors in overlapping imagery to match features across multiple images. Through non-linear least-squares minimization (Westoby et al., 2012), both camera positions and object coordinates are iteratively estimated in an arbitrary 3D coordinate system. Sparse bundle adjustment is implemented to transform measured image coordinates to three dimensional points of the area of interest. The outcome of this process is a sparse 3D point cloud in a local 3D coordinate system. Subsequently, through an incremental 3D scene reconstruction, the 3D point cloud is densified. Ground control points using GPS measurements are then used to georeference the 3D point cloud to a specific coordinate system. Through post-processing a digital surface model (DSM), and orthophotos are created. The target map area was modeled combining 7 separate SfM processing regions since hardware capacity could not handle the image dataset as one project. Depending on average distance from target surface mapped, the ground sampling distance varied from 1.9 cm/pixel to 12.85 cm/pixel. A total of 43 Ground Control Points (GCPs) were used to optimize camera parameters and georeference 3D point clouds. However, because the GCPs were not properly distributed throughout the model additional points from the LiDAR survey were used as GCPs.

Airborne Light Detection and Ranging (LiDAR) DSM and DTM

Airborne Light Detection and Ranging (LiDAR) data were generated by a company (AAM) following a request by a consortium of New Zealand agencies. The request for this study area came from GNS Science as multiple surface fault ruptures and landslides occurred in this area. The mapping involved multi-km² areas of the coastline and other areas of the north part of the South Island. A 2-laser channel Riegl Q1560 system was used with a scan angle of 58 degrees, multipulse mode and 370 kHz pulse rate. A target acquisition design of minimum 4 pulses per square meter (NPS) for each flightline swath was set with 50% minimum side overlap between adjacent swaths to ensure complete data coverage. To create the DTM, an automated classification scheme was used with additional manual classification editing to remove or add points to the ground class. The classified point cloud product contains the following classes: Default, Ground, Water. The generated 1 m DEM and DSM has a reported RMS of 0.053 m.

Results

Comparison of Satellite-based DSM with airborne LiDAR and UAV – SfM

Example of the data results using the three methods is shown in Figure 2 through 4. Figure 2 shows the LiDAR 1 m DEM and DSM of December 2016. Figure 3 shows a time sequence of SETSM Satellite DSM before the earthquake (March 23 2015), about a month after the earthquake (December 29 2016) and a few months after the earthquake (May 25 2017). Figure 4 illustrates the March 28-30 2017 UAV-enabled Structure-from-Motion DSM.

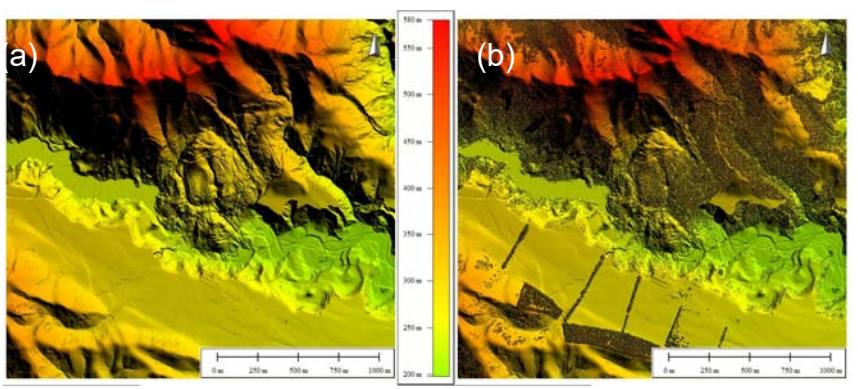


Figure 2. (a) LiDAR 1 m (a) DEM; (b) DSM conducted in December 2016.

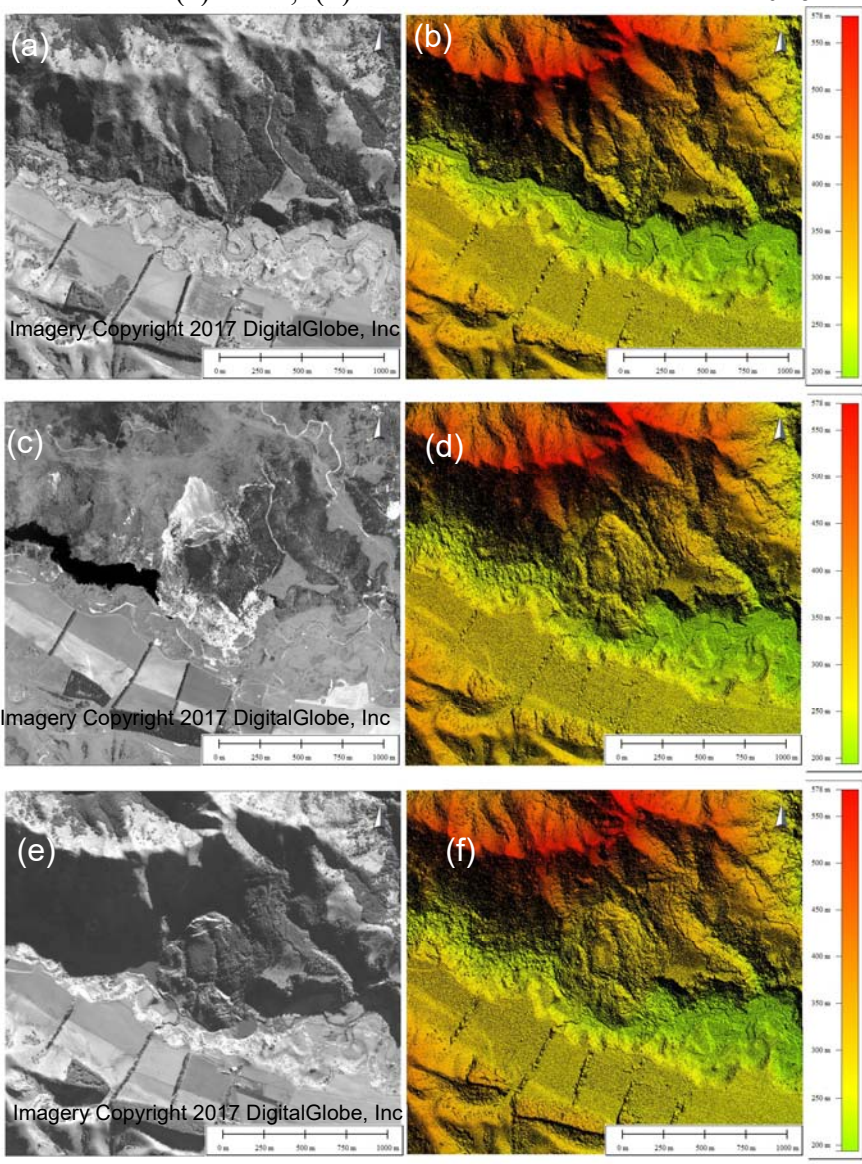


Figure 3. SETSM satellite orthophoto and DSM respectively (a, b) before the earthquake (March 23 2015); (c, d) on December 29 2016; and (e, f) on May 25 2017. DSMs created from DigitalGlobe, Inc. imagery.

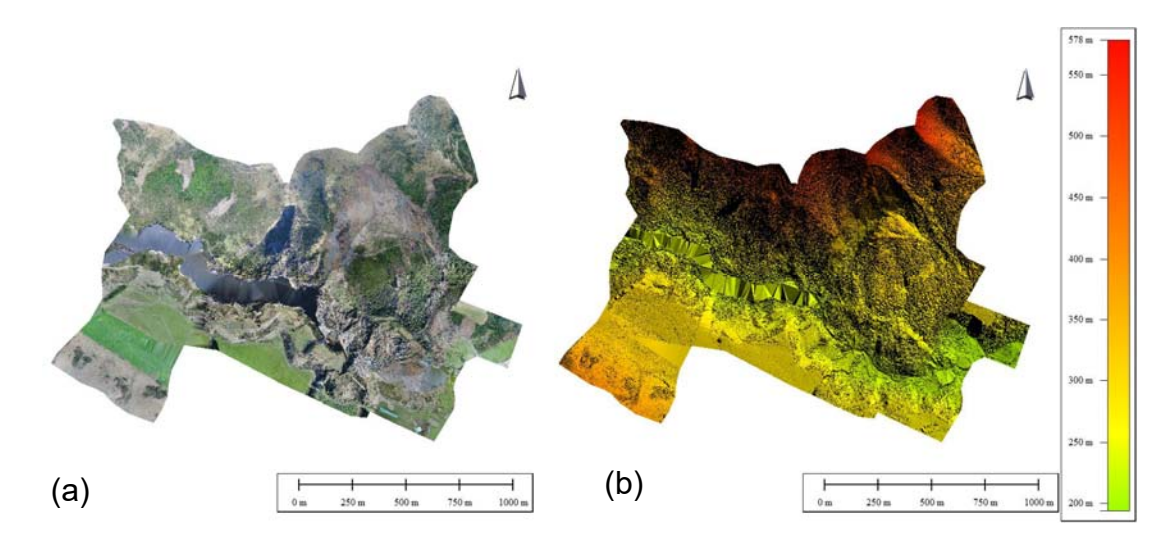


Figure 4. UAV-enabled SfM (a) orthophoto; and (b) DSM of March 28-30 2017.

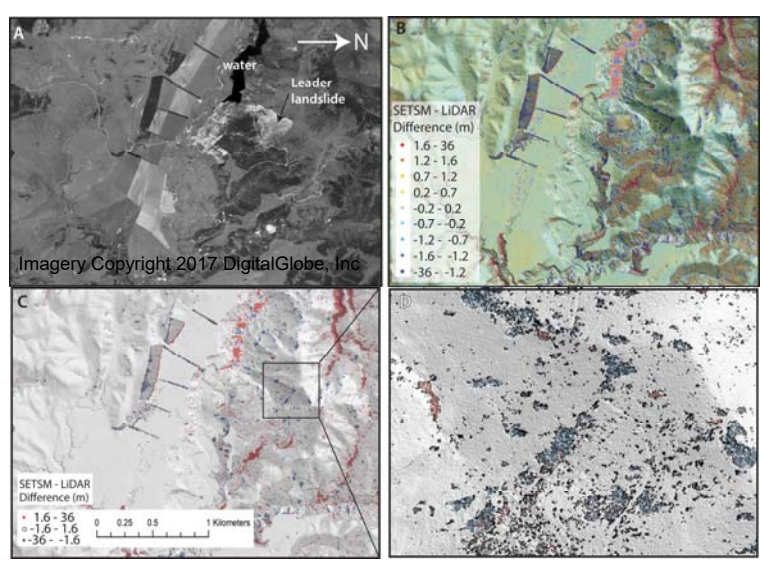


Figure 5. WorldView3 Satellite orthophoto (A) and raster difference model between SETSM DSM and LiDAR DSM in December 2016 (B and C). Panel D shows inset from panel C where red/blue patches identify differences larger than 1.6 m with black areas representing poor pixel image matching from satellite stereo pairs. Imagery Copyright 2016 DigitalGlobe, Inc. SETSM DSMs created from DigitalGlobe, Inc. imagery.

A comparison between the LiDAR DSM and the SETSM DSM in December 2016 is shown in Figure 5 as a difference raster draped over a hillshade with the accompanying orthophoto. Difference values have a mean of 0.03 m and a standard deviation of 1.4 m (Figure 5B). Max/min misfit values range from 36.0 to -35.4 m respectively. In sparsely vegetated areas (few trees, mostly grass), the difference is less than ~ 0.5 m. Larger difference values (> ± 1.6 m) are observed in small patches on steeper, sparsely vegetated slopes (Figure 5C), commonly up to 5 m. The highest difference values (up to 36 m) are associated with densely vegetated areas (on any slope) and with water ponded upstream of the Leader landslide within the Leader river. In particular, the largest positive difference values are located at the bottom of larger river valleys. Inspection of the

orthophoto reveals no cloud cover, but some significantly shadowed areas. However, areas of difference greater than ±1.6 m are associated with higher density "matchtag" points, which are flags generated by the SETSM routine for positions of poor image matching between the stereo pair scenes (Figure 5D). These are being used to guide filtering of the DSM data in current work. A comparison of the SETSM DSM of May 2017 with the SfM DSM of March 2017 is also shown in Fig. 6. The two models are similar (mean difference of -0.01 m and standard deviation of 1.97 m), but elevation differences of the order of 5 m are observed. These are attributed to registration errors with the SfM DSM, shadowed areas in the SETSM DSM, high-resolution mapped terrain features of the UAV model (GSD 1.91-12.85 cm/pix), which could cause larger differences when compared to the smoothed and lower resolution (50 cm grid size) SETSM DSM. Overall, these comparisons indicate that at the scales shown, and for areas of less steep terrain with no or little vegetation, the SETSM technique is generating reliable data of the 3D topography.

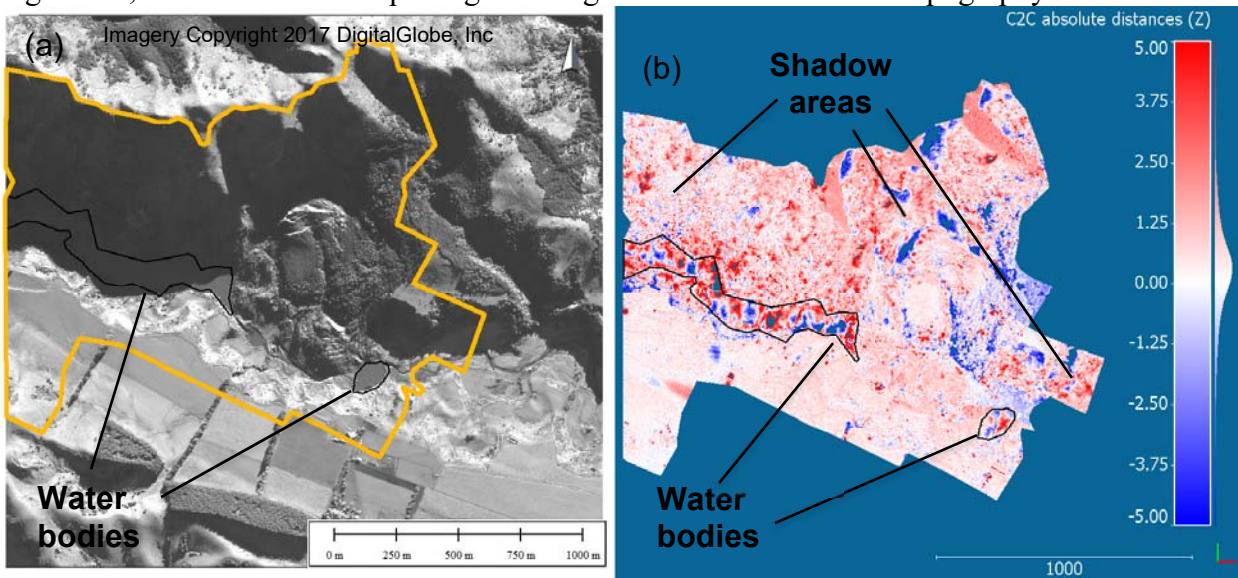


Figure 6. Satellite (a) orthophoto and (b) DEM of difference between UAV SfM DSM and SETSM DSM in March-May 2017. Imagery Copyright 2017 DigitalGlobe, Inc. SETSM DSMs created from DigitalGlobe, Inc. imagery.

Landslide Identification Using Pre-/ Post-event SETSM DSM Differencing

The developed SETSM DSMs were also differenced in an effort to assess the location and volume of the landslides and other mass movement features thought to have been initiated by the earthquake. Figure 7 shows the DEM of difference between the before the earthquake SETSM DSM (March 23 2015) and the after earthquake SETSM DSM (Dec 29 2016). A mean change of -0.12 m is observed through the area with a standard deviation of 5.7 m. The main Leader landslide is easily discerned, and exhibits a loss of height that reaches 66 m near the top part of the main Leader landslide and an increase in height of about 60 m due to the accumulation of the debris at the toe of the landslide. A cross-section through the landslide is also shown in Fig. 1 for the various 3D models. The pre-earthquake geometry from the SETSM DSM is visibly different to the post-earthquake DSM. The post-earthquake geometry is for many practical applications (e.g. stability assessment) identical for the UAV, SETSM and LiDAR DSM. Smaller changes on steep hillslopes are presumably related to shallow rock slides, although the vegetation and artifacts make identification of such features difficult and are the focus of ongoing filtering and processing.

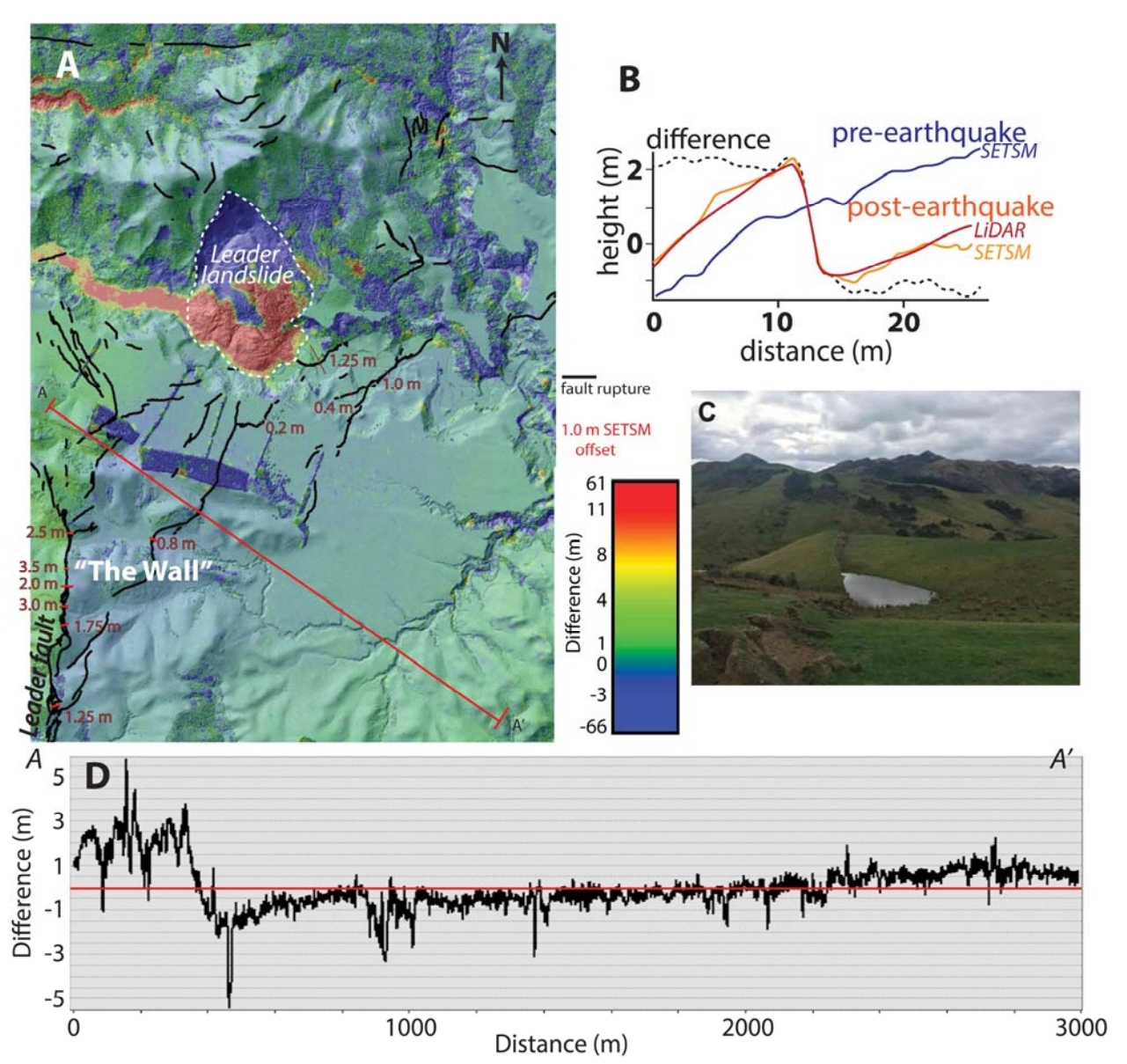


Figure 7. Surface change following the earthquake. (A) Difference raster based on March 2015 SETSM DSM and December 2016 SETSM DSM draped over hillshade, numbers indicate vertical offset; (B) and (C) Profile section and field photograph (photo by T. Stahl) showing vertical displacement at "The Wall" along Leader fault; D) Longwavelength tilt of eastern fault block shows 2 m subsidence toward the fault over 3 km length. SETSM DSMs created from DigitalGlobe, Inc. imagery.

The Humps Fault Zone and the South Leader Fault

In addition to the observed landslides, significant surface rupturing faults are present and clearly identifiable by the SETSM difference model in the Leader valley (Figure 7). The Leader landslide marks the approximate location of the complex damage zone at the intersection of The Humps Fault Zone (the hypocentral fault of the Kaikoura earthquake) and the Leader Fault Zone (Nicol et al. 2018). The complex fault kinematics between these two fault zones, the relatively weak Tertiary geologic formations located along the faults, and surface rupture interactions with topography have

led to a pronounced vertical component of faulting in and around the Leader valley. Field teams mapped the faults and hand-measured displacements (estimated \pm 0.25 m uncertainty) within three weeks of the earthquake; RTK and dGPS surveying was conducted later, after farm operations resumed and destroyed some fault scarps. These field data allow us to directly evaluate the SETSM difference model.

South of the landslide site, the "Wall of Waiau" fault trace (hereafter referred to as the "Wall", so named for its prominent ~3.5 m vertical face) traverses a south-trending ridge that consists of Miocene age siltstone (Figure 7 B and C). The Wall is part of a N-trending, ~100 m-wide sinistral shear zone with a near-vertical dip that variably renders the fault normal or reverse (as evidenced by projection of the trace across topography). Up to ~3 m of sinistral and 3.5 m of vertical displacement were recorded along the fault trace in the field, commensurate with the orientation sinistral-reverse and sinistral-normal strike that decorate the scarp face (Nicol et al. 2018). These offsets are reproducible at six measured fault sections in the SETSM difference raster over offsets that range from 1.25 m to 3.5 m (Figure 7A). Some of the vertical component is likely to be influenced by gravitational failure and/or secondary bending stresses within the hanging wall of frontal thrusts. The fact that displacement is localized at this sharp boundary in the DSM model, and that subsidence is greater than uplift, might be evidence that this rupture is in part due to slope failure.

There are three fault traces that are buried or have been exposed by subsequent post-breach incision into the Leader Landslide. One trace virtually coincides with the toe of the landslide, but continues along the rangefront and is therefore tectonic. Displacement measurements were made throughout the area in the field. These discrete displacement measurements and the displacements using SETSM differencing are in very good agreement, as shown in Figure 8.

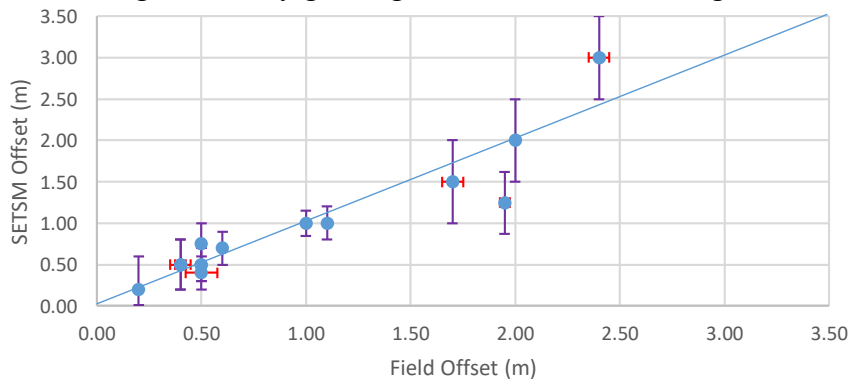


Figure 8. Comparison of fault rupture offset from field measurements and SETSM.

Conclusions

Digital surface models derived from Surface Extraction with TIN-based Search-space Minimization (SETSM) technique are shown to have sub-meter accuracy when compared to LiDAR and UAV-photogrammetry techniques. Measured terrain changes, including landslides and fault offsets, demonstrate suitability for post-earthquake analyses via satellite imagery, especially where pre-event, high-resolution topography datasets are lacking. The technique still has limitations that are being investigated. In addition to the inability to map the ground surface in densely vegetated or water-covered areas, which is a known limitation of photogrammetric-based techniques, it appears to underestimate the depth of narrow valleys, and also is prone to generate a spurious noise with an amplitude of ± 0.25 m.

Acknowledgements

The work is funded through a National Science Foundation (NSF) RAPID Grant No. EAR-1719496 and EAR-1719524. Any opinions, findings, and conclusions or recommendations expressed in this material are those of the authors and do not necessarily reflect the views of the NSF. We thank Paul Morin from the PGC (Polar Geospatial Center) for providing imagery access and support for acquiring Digital Globe satellite data through a NGA (National Geospatial-Intelligence Agency) cooperative agreement with NSF (NextView License), which is supported by NSF grants OPP-1043681, OPP-1559691 and OPP-1542736. Geospatial support for this work was provided by the Polar Geospatial Center under NSF awards EAR-1719496 and EAR-1719524. This research is part of the Blue Waters sustained-petascale computing project, which is supported by NSF (awards OCI-0725070 and ACI-1238993) and the state of Illinois. Blue Waters is a joint effort of the University of Illinois at Urbana-Champaign and its National Center for Supercomputing Applications. All images are the copyright of Digital Globe, 2017. We also thank GNS Science and New Zealand's Natural Hazards Research Platform for funding the airborne LIDAR acquisition for the study area.

References

- 1. Dellow, S., Massey, C., Cox, S., Archibald, G., Begg, J., Bruce, Z., Carey, J. Davidson, J., Della Pasqua, F., Glassey, P., Hill, M., Jones, K., Lyndsell, B., Lukovic, B. McColl, S., Rattenbury, M., Read, S., Rosser, B., Singeisen, C. Townsend, D., Villamor, P. Villeneuve2, M., Wartman, J., Rathje, E., Sitar, N., Athanasopoulos-Zekkos A. Manousakis, J., and Little, M., Landslides caused by the Mw 7.8 Kaikoura Earthquake and the immediate response, Bulletin of the New Zealand Society for Earthquake Engineering, 2017, 50 (2), 106-116.
- 2. GEER, Geotechnical reconnaissance of the 2016 Mw 7.8 Kaikoura, New Zealand earthquake, Version 1.0, June 2017.
- 3. Hamling, I.J.; Hreinsdottir, S.; Clark, K.J.; Elliot, J.; Liang, C.; Fielding, E.; Litchfield, N.J.; Villamor, P.; Wallace, L.M.; Wright, T.J.; D'Anastasio, E.; Bannister, S.C.; Burbidge, D.R.; Denys, P.; Gentle, P.; Howarth, J.D.; Mueller, C.; Palmer, N.G.; Pearson, C.; Power, W.L.; Barnes, P.; Barrell, D.J.A.; Van Dissen, R.J.; Langridge, R.M.; Little, T.; Nicol, A.; Pettinga, J.; Rowland, J.; Stirling, M.W. Complex multifault rupture during the 2016 Mw 7.8 Kaikoura earthquake, New Zealand. 2017, Science, 356(6334): eaam7194; doi: 10.1126/science.aam7194.
- 4. Massey, C. I., Townsend, D., Rathje, E., Allstadt, K., Kaneko, Y., Lukovic, B., Bradley, B., Wartman, J., Horspool, N., Hamling, I., Carey, J., Cox, S., Davidson, J., Dellow, S., Godt, J., Holden, C., Jibson, R., Jones, K., Kaiser, A., Little, M. Lyndsell, B., McColl, S., Morgenstern, R., Petley, D. N., Rengers, F., Rhoades, D., Rosser, B., Strong, D., Singeisen, C., Villeneuve, M. Landslides triggered by the MW 7.8 14 November 2016 Kaikoura Earthquake, New Zealand. In review. Bulletin of the Seismological Society of America.
- 5. Nicol, A., Khajavi, N., Pettinga, J., Fenton, C., Stahl, T., Bannister, S., Pedley, K., Hyland, N., Bushell, T., Hamling, I., Ristau, J., Noble, D., McColl, S. Preliminary geometry, slip and kinematics of fault ruptures during the 2016 MW 7.8 Kaikōura Earthquake in the North Canterbury region of New Zealand. Submitted to Bulletin of the Seismological Society of America, Kaikoura Earthquake Special Issue.
- 6. Noh, M.J., I.M. Howat. Automated stereo-photogrammetric DEM generation at high latitudes: Surface Extraction from TIN-Based Search Minimization (SETSM) validation and demonstration over glaciated regions, *GIScience and Remote Sensing*, 2015 doi:10.1080/15481603.2015.1008621.
- 7. Noh, M. J., I.M. Howat. Surface Extraction from TIN based Search-space Minimization (SETSM) algorithm, International Society for Photogrammetry and Remote Sensing (ISPRS) Journal of Photogrammetry and Remote Sensing, 2017; 129: 55-76.
- 8. Schenk, T.F. Digital Photogrammetry. Published by TerraScience, Laurelville, OH, 1999.
- 9. Shean, D. E., O. Alexandrov, Z. Moratto, B. E. Smith, I. R. Joughin, C. C. Porter, Morin, P. J., An automated, open-source pipeline for mass production of digital elevation models (DEMs) from very high-resolution commercial stereo satellite imagery, *ISPRS J. Photogramm. Remote Sens*, 2016; **116**: 101-117, doi: 10.1016/j.isprsjprs.2016.03.012, 2016.
- 10. Westoby, M. J., Brasington, J., Glasser, N. F., Hambrey, M. J., & Reynolds, J. M. 'Structure-from-Motion' photogrammetry: A low-cost, effective tool for geoscience applications. *Geomorphology*, 2012; **179**: 300-314.
- 11. Willis, M.J., Herried, B.G., Bevis, M.G and Bell, R.E. Recharge of a subglacial lake by surface meltwater in northeast Greenland. *Nature*, 2015; **518**: 223-227 doi:10.1038/nature14116